Noname manuscript No.
(will be inserted by the editor)

SENSOR CONFIGURATION TRADE STUDY FOR NAVIGATION IN NEAR RECTILINEAR HALO ORBITS

Sehyun Yun · Kirsten Tuggle · Renato Zanetti · Christopher D'Souza

the date of receipt and acceptance should be inserted later

Abstract Deep Space Gateway is a NASA program planned to support deep space human exploration and prove new technologies needed to achieve it. One Gateway requirement is the ability to operate in the absence of communications with the Deep Space Network (DSN) for a period of at least three weeks. In this paper, three types of onboard sensors (a camera for optical navigation, a GPS receiver, and X-ray navigation) are considered to enhance its autonomy and reduce the reliance on DSN. A trade study is conducted to explore alternatives on how to achieve autonomy and how to reduce DSN dependency while satisfying navigation performance requirements. Using linear covariance analysis, error budgets, and sensitivity analysis, the performance of navigation systems using combinations of DSN with the aforementioned onboard sensors is shown.

Keywords

Navigation, Linear Covariance Analysis, Orbit Determination

1 Introduction

NASA's Gateway is planned to be a fundamental step in returning to the Moon and embarking on crewed missions beyond the Earth-Moon system. Gateway is meant to be a spaceport and center for research in order to support a human presence on the Moon and prove new technologies for deep space

---

Sehyun Yun, Kirsten Tuggle, and Renato Zanetti
Department of Aerospace Engineering and Engineering Mechanics, The University of Texas at Austin, Austin, TX 78712. Corresponding author: Renato Zanetti renatoutexas.edu

Christopher D'Souza
Aeroscience and Flight Mechanics Division, NASA Johnson Space Center EG6, 2101 NASA Parkway, Houston, Texas, 77058.

exploration. Due to a number of favorable properties, a Near Rectilinear Halo Orbit (NRHO)[1] has been selected for the Gateway's trajectory. As components such as a habitat and other modules are delivered, Gateway will traverse its baseline NRHO in both crewed and uncrewed scenarios. It has been assumed that the primary resource for tracking and determining Gateway's orbit at all times will be the Deep Space Network (DSN).[2] Recent work[3] has assessed the extent to which the DSN should be utilized to meet the tracking requirements for orbit determination, in both crewed and uncrewed situations. In the uncrewed case, the DSN was assumed to be the only observation source. The current work is a trade study to reduce dependency on DSN by replacing some or all DSN passes with different types of onboard measurements.

An NRHO Gateway reference trajectory has been provided[3] externally for the study. Minimal thrusting is expected in the uncrewed scenario beyond small orbit maintenance maneuvers. This is in contrast to the crewed scenario where it is expected that large forces will be exerted due to venting associated with crew operations. This work begins by identifying sensor types that can be reasonably expected for use on Gateway. Since the objective is orbit determination, these sensors must produce indirect or direct observations of inertial position and velocity. Attitude determination will still be necessary, even in the uncrewed scenario, since Gateway is expected to maintain a solar pressure equilibrium attitude (SPEA). That, however, is irrelevant to the current problem since DSN provides no attitude information. For each option in the trade space, the number of DSN passes required to meet orbit determination requirements is characterized. The sensing options selected are: a camera for optical navigation, GPS, and X-ray navigation.[4] The optical camera option here specifically indicates processing of centroid and apparent diameter measurements in order to reflect use of existing Orion optical navigation algorithms.[5] The increased size of Gateway, compared to say the Orion spacecraft, opens up the possibility for accommodating a high-gain antenna for GPS signals.

A number of recent contributions exist that explore potential advantages of different onboard sensors for vehicles in a Gateway-like orbit.[1,6–10] Ref. 1 explores navigation improvements to the crewed scenario using only optical navigation processing centroid and apparent diameter measurements. Ref. 6 provides performance results when optical feature tracking is used in concert with DSN passes. New navigation packages DPS-Navigator and the Cislunar Autonomous Positioning System (CAPS) are developed and examined in Refs. 6 and 8, respectively. Ref. 9 offers feasible navigation performance using GNSS signals at lunar NRHO distances from Earth. Since the aim of this paper was viability of the concept in general, it did not include trades on DSN passes. Ref. 10 is most similar to the current work. There, navigation performance was examined for the sensing options of lunar beacons, X-ray pulsar navigation, and optical navigation using centroids and apparent diameters. However, since autonomy was the chief goal in that work, performance was evaluated in the context of avoiding DSN altogether.

This work seeks to characterize how utilizing different sensor types can alleviate the load of DSN, with the ultimate goal of more efficiently managing DSN resources. Trade options are provided for different levels of DSN reliance (including complete autonomy), and the study will be restricted to sensors which only require modest additions to Orion hardware and software. The analysis is performed using Linear Covariance techniques.[11, 12] While this approach provides less precise values for the absolute uncertainty of each navigation configuration than high-fidelity Monte Carlo simulations, it allows for rapid evaluation of large trade spaces and quickly provides trends of different navigation design options with accurate measures of the relative contributions of each data type.

2 Models

2.1 States

The state vector utilized is:

$$\mathbf{x} = \begin{bmatrix} \mathbf{r}_{\text{GM}} \\ \mathbf{v}_{\text{GM}} \end{bmatrix} \tag{1}$$

where $\mathbf{r}_{\text{GM}}$ and $\mathbf{v}_{\text{GM}}$ respectively represent the position and velocity of the Gateway spacecraft with respect to the center of the Moon in inertial coordinates (J2000).

The provided nominal trajectory , denoted $\bar{\mathbf{x}}$, is one that is currently baselined for Gateway about the Earth-Moon L2 point.[6] It is a member of a class of orbits known as Near Rectilinear Halo Orbits (NRHOs). In the Earth-Moon rotating frame, the orbit is quasi-periodic in a 9:2 resonance with the lunar synodic period, yielding an orbital period of approximately 6.5 days. Since the orbit is slightly unstable, meaning that in the long term the natural dynamics of the system would result in Gateway departing the vicinity of the Moon, small stationkeeping maneuvers are applied (generally at apolune). Apolune and perilune radii for the trajectory are approximately 70,000 km and 3200 km, respectively. Figure 1 shows nominal positions of Gateway with respect to the Moon in the Earth-Moon rotating frame over the course of about 1 month. The initial epoch is January 5, 2020 16:19:41.472 (UTC), with the following initial conditions (in J2000):

$$\begin{aligned} \bar{\mathbf{r}}_{\text{GM}}(t_0) &= \begin{bmatrix} 4825.71 \; 34473.03 \; -62479.95 \end{bmatrix}^T \text{km} \\ \bar{\mathbf{v}}_{\text{GM}}(t_0) &= \begin{bmatrix} 0.0482217 \; -0.0480778 \; -0.0226442 \end{bmatrix}^T \text{km/s} \end{aligned} \tag{2}$$

A navigation simulation can be performed by implementing a Kalman filter acting on the system for $\mathbf{x}$ after linearization about the nominal trajectory, $\bar{\mathbf{x}}$. In particular, we will examine the first-order evolution of the error covariance associated with this estimator over time and measurement updates for different candidate sensor systems.

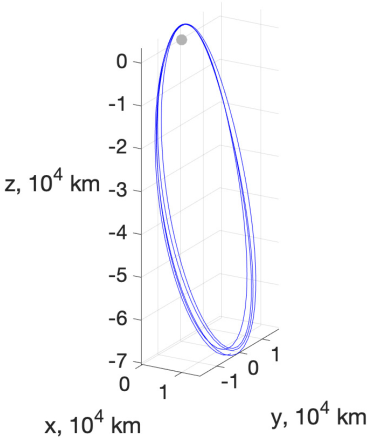

3-D Trajectory

Fig. 1: 3-D Nominal Position in Earth-Moon Rotating Frame, km

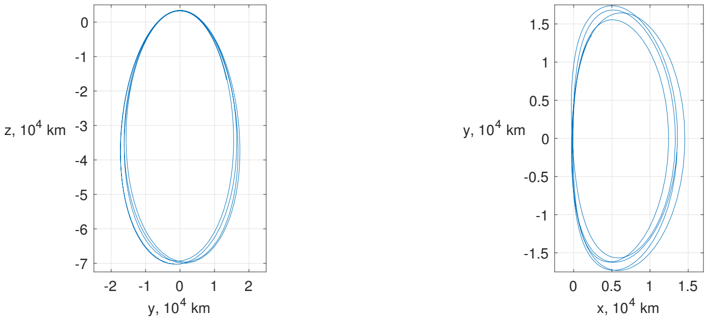

2-D Trajectory, z vs. y

2-D Trajectory, y vs. x

Fig. 2: 2-D Nominal Position in Earth-Moon Rotating Frame, km

We denote deviations of the true state from the nominal as $\delta\mathbf{x} = \mathbf{x} - \bar{\mathbf{x}}$ and of the estimated state from the nominal as $\delta\hat{\mathbf{x}} = \hat{\mathbf{x}} - \bar{\mathbf{x}}$. The difference in how the true and estimated states deviate from the nominal is $\delta\mathbf{e} = \delta\mathbf{x} - \delta\hat{\mathbf{x}}$. The estimation error and its covariance are then:

$$\mathbf{e} = \mathbf{x} - \hat{\mathbf{x}} = \mathbf{x} - \bar{\mathbf{x}} - (\hat{\mathbf{x}} - \bar{\mathbf{x}}) = \delta\mathbf{x} - \delta\hat{\mathbf{x}} = \delta\mathbf{e} \tag{3}$$

$$P = \mathbb{E}\{\mathbf{e}\mathbf{e}^T\} = \mathbb{E}\{\delta\mathbf{e}\delta\mathbf{e}^T\} \tag{4}$$

Note that use of a Kalman filter linearized about the provided nominal trajectory rather than an extended Kalman filter results in error covariance updates depending only on the nominal trajectory - not the state estimates themselves

- since the Jacobians governing these linear updates are evaluated only at the nominal trajectory.

2.2 Initial Uncertainties and Navigation Requirements

The filter uncertainty is initialized using the orbital insertion error statistics below:

	3-σ Initial RSS Value
Position	20 km
Velocity	20 cm/s

with initial cross-correlations of 0 for and between position and velocity. These values, from Ref. 7, correspond to orbital insertion errors at apolune (where our nominal trajectory begins). Navigation performance requirements are to maintain 3-σ RSS values of 10 km and 10 cm/s for position and velocity, respectively.[3]

2.3 Deterministic Dynamics

The filter dynamics directly incorporate gravitational accelerations due to the Earth, Moon, and Sun. The Earth and the Sun are treated as point masses or equivalently as spheres with radially symmetric density.

$$
\begin{aligned}
\begin{bmatrix} \dot{\mathbf{r}}_{\mathrm{GM}} \\ \dot{\mathbf{v}}_{\mathrm{GM}} \end{bmatrix} &= \mathbf{f}(\mathbf{x}, t) \\
&= \begin{bmatrix} \mathbf{v}_{\mathrm{GM}} \\ \mathbf{a}_{\mathrm{GI}} - \mathbf{a}_{\mathrm{MI}} \end{bmatrix} \\
&= \begin{bmatrix} \mathbf{v}_{\mathrm{GM}} \\ -\frac{\mu_E}{\|\mathbf{r}_{\mathrm{GE}}\|^3}\mathbf{r}_{\mathrm{GE}} - \frac{\mu_S}{\|\mathbf{r}_{\mathrm{GS}}\|^3}\mathbf{r}_{\mathrm{GS}} - \frac{\mu_M}{\|\mathbf{r}_{\mathrm{GM}}\|^3}\mathbf{r}_{\mathrm{GM}} - \mathbf{a}_{\mathrm{MI}} \end{bmatrix}
\end{aligned}
\tag{5}
$$

Since this linearized filter operates on a predefined nominal trajectory and the task at hand is one of linear covariance (LinCov) analysis, these dynamics are not used directly. Rather, the associated dynamics Jacobian is used to govern the evolution of the uncertainty.

$$
F(\bar{\mathbf{x}}, t) = \begin{bmatrix} 0_{3\times3} & \mathrm{I}_3 \\ G_{\mathrm{M}}(\bar{\mathbf{r}}_{\mathrm{GM}}) + G_E(\bar{\mathbf{r}}_{\mathrm{GE}}) + G_{\mathrm{S}}(\bar{\mathbf{r}}_{\mathrm{GS}}) & 0_{3\times3} \end{bmatrix}
\tag{6}
$$

where

$$
\begin{aligned}
G_{\mathrm{M}}(\bar{\mathbf{r}}_{\mathrm{GM}}) &= \mu_{\mathrm{M}} \left(3\frac{[\bar{\mathbf{r}}_{\mathrm{GM}}][\bar{\mathbf{r}}_{\mathrm{GM}}]^T}{\|\bar{\mathbf{r}}_{\mathrm{GM}}\|^5} - \frac{1}{\|\bar{\mathbf{r}}_{\mathrm{GM}}\|^3}\mathrm{I}_3 \right) \\
G_{\mathrm{E}}(\bar{\mathbf{r}}_{\mathrm{GE}}) &= \mu_E \left(3\frac{[\bar{\mathbf{r}}_{\mathrm{GE}}][\bar{\mathbf{r}}_{\mathrm{GE}}]^T}{\|\bar{\mathbf{r}}_{\mathrm{GE}}\|^5} - \frac{1}{\|\bar{\mathbf{r}}_{\mathrm{GE}}\|^3}\mathrm{I}_3 \right) \\
G_{\mathrm{S}}(\bar{\mathbf{r}}_{\mathrm{GS}}) &= \mu_S \left(3\frac{[\bar{\mathbf{r}}_{\mathrm{GS}}][\bar{\mathbf{r}}_{\mathrm{GS}}]^T}{\|\bar{\mathbf{r}}_{\mathrm{GS}}\|^5} - \frac{1}{\|\bar{\mathbf{r}}_{\mathrm{GS}}\|^3}\mathrm{I}_3 \right)
\end{aligned}
\tag{7}
$$

and

$$\begin{aligned}\bar{\mathbf{r}}_{\mathrm{GE}} &= \bar{\mathbf{r}}_{\mathrm{GM}} - \mathbf{r}_{\mathrm{EM}} \\ \bar{\mathbf{r}}_{\mathrm{GS}} &= \bar{\mathbf{r}}_{\mathrm{GM}} - \mathbf{r}_{\mathrm{SM}}\end{aligned} \tag{8}$$

utilizes the ephemerides of the Earth, Moon, and Sun available in SPICE.[13]

2.4 Uncertain Dynamics / Process Noise

Ideally, all dynamical perturbations would be explicitly modeled in a navigation filter, but the computationally constrained nature of onboard filtering precludes this possibility. Since the purpose of this study is utilization of onboard resources, we therefore choose to be consistent in treatment of certain perturbation sources as process noise. These sources were: burn execution errors, desaturation perturbations, and solar radiation pressure (SRP).[14] Process noise values due to burn imperfections were modeled as in Ref. 3, using 3-σ RSS values of 1.42 mm/s and 1.5% for an additive noise term and scale factor term, respectively. A 3-σ RSS value of 3 cm/s was used for desaturation perturbations.[3] For solar radiation pressure, a constant power spectral density of $Q = 5.5 \times 10^{-15}\mathrm{I}_3 \ \frac{m^2}{s^3}$ was applied to velocity uncertainties over time.[10]

3 Observation Models

3.1 DSN Measurement Model

The DSN is generally utilized for deep space missions. It assists navigation of spacecraft far from Earth with range and range-rate measurements along the line of sight (LOS) from the ground station to the vehicle. The DSN consists of three deep space communications facilities located roughly 120° apart around the world: at Goldstone (California, USA), Madrid (Spain), and Canberra (Australia).

The range measurement is expressed as follows:

$$h_{\mathrm{range}}(\mathbf{x}) = \|\mathbf{r}_{\mathrm{GE}} - \mathbf{r}_{\mathrm{GSE}}\| + \nu_{\mathrm{range}} = \|\mathbf{r}_{\mathrm{GM}} + \mathbf{r}_{\mathrm{ME}} - \mathbf{r}_{\mathrm{GSE}}\| + \nu_{\mathrm{range}} \tag{9}$$

where $\|\cdot\|$ is the vector Euclidian norm and $\mathbf{r}_{\mathrm{GSE}}$ is the position vector of the ground station with respect to Earth in the inertial frame. Note that this model is high-level, meaning it corresponds to the expected quality of a range measurement outputted from the DSN measurement system. System-level considerations such as iterative solutions for light-time, etc., are ignored for this study. Since h_{range} is invariant to the origin or orientation of the coordinate frame used, there exist multiple, equivalent expressions for Eq. (9). The linearized range measurement model is described as

$$H_{\mathrm{range}}(\bar{\mathbf{x}})\delta\mathbf{x} = \frac{(\bar{\mathbf{r}}_{\mathrm{GM}} + \mathbf{r}_{\mathrm{ME}} - \mathbf{r}_{\mathrm{GSE}})^{\mathrm{T}}}{\|\bar{\mathbf{r}}_{\mathrm{GM}} + \mathbf{r}_{\mathrm{ME}} - \mathbf{r}_{\mathrm{GSE}}\|}\delta\mathbf{r}_{\mathrm{GM}} \tag{10}$$

and the discrete range measurement noise sequence is modeled as:

$$\nu_{\text{range}} \overset{\text{i.i.d}}{\sim} N(0\text{ m}, 1\text{ m}^2) \tag{11}$$

where $N(\mu, \sigma^2)$ represents the Gaussian pdf with mean μ and covariance σ^2.

The range-rate measurement is obtained by differentiating Eq. (9) with respect to time.

$$h_{\text{range-rate}}(\mathbf{x}) = \frac{(\mathbf{r}_{\text{GM}} + \mathbf{r}_{\text{ME}} - \mathbf{r}_{\text{GSE}})^{\text{T}}((\mathbf{v}_{\text{GM}} + \mathbf{v}_{\text{ME}} - \mathbf{v}_{\text{GSE}})}{\|(\mathbf{r}_{\text{GM}} + \mathbf{r}_{\text{ME}} - \mathbf{r}_{\text{GSE}})\|} + \nu_{\text{range-rate}} \tag{12}$$

where all velocities represent the time rate of change of the position vector with respect to the inertial frame. The linearized range-rate measurement model is expressed as follows:

$$H_{\text{range-rate}}(\bar{\mathbf{x}})\delta\mathbf{x} = \begin{bmatrix} \frac{\partial h_{\text{range-rate}}}{\partial \mathbf{r}_{\text{GM}}}(\bar{\mathbf{x}}) & \frac{\partial h_{\text{range-rate}}}{\partial \mathbf{v}_{\text{GM}}}(\bar{\mathbf{x}}) \end{bmatrix} \begin{bmatrix} \delta\mathbf{r}_{\text{GM}} \\ \delta\mathbf{v}_{\text{GM}} \end{bmatrix} \tag{13}$$

where

$$\begin{aligned} \frac{\partial h_{\text{range-rate}}}{\partial \mathbf{r}_{\text{GM}}}(\bar{\mathbf{x}}) = & \frac{(\bar{\mathbf{v}}_{\text{GM}} + \mathbf{v}_{\text{ME}} - \mathbf{v}_{\text{GSE}})^{\text{T}}}{\|(\bar{\mathbf{r}}_{\text{GM}} + \mathbf{r}_{\text{ME}} - \mathbf{r}_{\text{GSE}})\|} \\ & \cdot \left[\mathrm{I}_{3\times 3} - \frac{(\bar{\mathbf{r}}_{\text{GM}} + \mathbf{r}_{\text{ME}} - \mathbf{r}_{\text{GSE}})(\bar{\mathbf{r}}_{\text{GM}} + \mathbf{r}_{\text{ME}} - \mathbf{r}_{\text{GSE}})^{\text{T}}}{\|(\mathbf{r}_{\text{GM}} + \mathbf{r}_{\text{ME}} - \mathbf{r}_{\text{GSE}})\|^2} \right] \end{aligned} \tag{14}$$

$$\frac{\partial h_{\text{range-rate}}}{\partial \mathbf{v}_{\text{GM}}}(\bar{\mathbf{x}}) = \frac{(\bar{\mathbf{r}}_{\text{GM}} + \mathbf{r}_{\text{ME}} - \mathbf{r}_{\text{GSE}})^{\text{T}}}{\|(\bar{\mathbf{r}}_{\text{GM}} + \mathbf{r}_{\text{ME}} - \mathbf{r}_{\text{GSE}})\|} \tag{15}$$

and the range-rate measurement noise sequence is modeled as:

$$\nu_{\text{range-rate}} \overset{\text{i.i.d}}{\sim} N(0\text{ mm}, 1\text{ mm}^2) \tag{16}$$

Although accurate position and velocity can be estimated using DSN, it requires sizeable ground operation and scheduling to coordinate the observations. The measurement models for different sensor types such as optical, GPS, and X-ray are used to reduce the demand for DSN in this study.

3.2 Optical Measurement Model

The centroid and apparent diameter of the Moon as imaged onboard Gateway depend on the relative position between Gateway and the Moon. The Orion image processing algorithm[5] utilizes a pinhole camera model to produce these measurements. Figure 3 illustrates this concept. This optical camera measurement model and a linear form with respect to the states of Gateway will now be presented.

$$\mathbf{r}_{\text{MC}}^{\text{C}} = -\mathbf{T}_{\text{I}}^{\text{C}}(\epsilon_{\text{C}})\left(\mathbf{r}_{\text{GM}} + \mathbf{r}_{\text{CG}}\right) \tag{17}$$

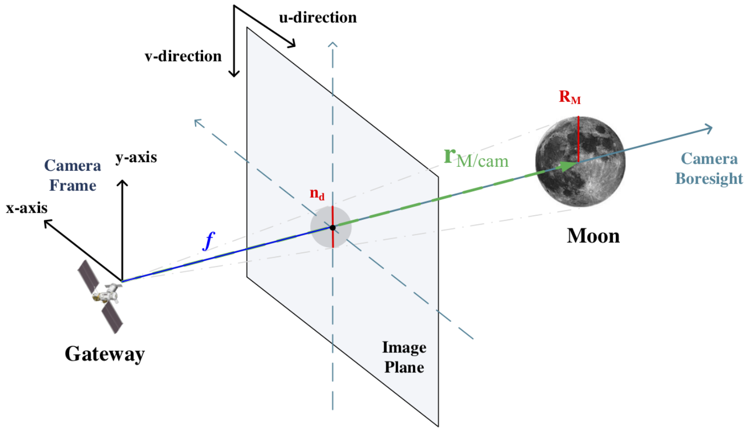

Fig. 3: Concept of Optical Camera Measurements

where $\mathbf{r}_{\mathrm{MC}}^{\mathrm{C}}$ is the position vector of the Moon with respect to the camera in the camera frame, $\mathbf{T}_{\mathrm{I}}^{\mathrm{C}}$ is the transformation matrix from inertial coordinates to camera coordinates, ϵ_{C} is the misalignment of the camera frame with respect to the Gateway body frame, and $\mathbf{r}_{\mathrm{CG}}$ is the position vector of the camera with respect to the origin of the Gateway body frame in inertial coordinates. Then, the variation of Eq. (17) is expressed as follows:

$$\delta \mathbf{r}_{\mathrm{MC}}^{\mathrm{C}} = -\delta \mathbf{T}_{\mathrm{I}}^{\mathrm{C}}(\epsilon_{\mathrm{C}})\left(\mathbf{r}_{\mathrm{GM}} + \mathbf{r}_{\mathrm{CG}}\right) - \mathbf{T}_{\mathrm{I}}^{\mathrm{C}} \delta \mathbf{r}_{\mathrm{GM}} - \mathbf{T}_{\mathrm{I}}^{\mathrm{C}} \delta \mathbf{r}_{\mathrm{CG}} \tag{18}$$

The measurement model for Moon centroid is given by

$$\begin{bmatrix} u \\ v \end{bmatrix} = -\frac{fs}{z_{\mathrm{MC}}^{\mathrm{C}}} \begin{bmatrix} x_{\mathrm{MC}}^{\mathrm{C}} \\ y_{\mathrm{MC}}^{\mathrm{C}} \end{bmatrix} + \begin{bmatrix} u_{\mathrm{c}} \\ v_{\mathrm{c}} \end{bmatrix} \tag{19}$$

where u and v are the camera measurements, u_{c} and v_{c} are the coordinates of the center of the focal plane array, f is the camera focal length (35.1 mm), and s is the inverse of the pixel pitch ($1/s = 4.8 \times 10^{-6}$ m/pixel).

LinCov analysis employs linearization to compute the error covariance matrices. This linearization is performed centered at the nominal value of the state; hence the Jacobian matrices of the nonlinear dynamic and measurement functions are evaluated at the nominal state. For the purpose of this work, it is assumed that during optical navigation passes the nominal attitude of Gateway is such that the camera points exactly at the center of the Moon, i.e. $x_{\mathrm{MC}}^{\mathrm{C}} = y_{\mathrm{MC}}^{\mathrm{C}} = 0$.

The variation of the pixel location with respect to the position vector of the camera in camera frame can be obtained as follows:

$$\begin{bmatrix} \delta u \\ \delta v \end{bmatrix} = -\frac{fs}{z_{\mathrm{MC}}^{\mathrm{C}}} \begin{bmatrix} 1 & 0 & -x_{\mathrm{MC}}^{\mathrm{C}}/z_{\mathrm{MC}}^{\mathrm{C}} \\ 0 & 1 & -y_{\mathrm{MC}}^{\mathrm{C}}/z_{\mathrm{MC}}^{\mathrm{C}} \end{bmatrix} \delta \mathbf{r}_{\mathrm{MC}}^{\mathrm{C}} = \begin{bmatrix} \mathbf{c}_1^T \\ \mathbf{c}_2^T \end{bmatrix} \delta \mathbf{r}_{\mathrm{MC}}^{\mathrm{C}} \tag{20}$$

Then, the partials of the Moon centroid measurements are described as:

$$\frac{\partial u}{\partial \mathbf{r}_{\mathrm{GM}}} = \frac{\partial u}{\partial \mathbf{r}_{\mathrm{MC}}^{\mathrm{C}}} \frac{\partial \mathbf{r}_{\mathrm{MC}}^{\mathrm{C}}}{\partial \mathbf{r}_{\mathrm{GM}}} = -\mathbf{c}_1^T \mathbf{T}_{\mathrm{I}}^{\mathrm{C}} \tag{21}$$

$$\frac{\partial u}{\partial \epsilon_{\mathrm{C}}} = \frac{\partial u}{\partial \mathbf{r}_{\mathrm{MC}}^{\mathrm{C}}} \frac{\partial \mathbf{r}_{\mathrm{MC}}^{\mathrm{C}}}{\partial \epsilon_{\mathrm{C}}} = \mathbf{c}_1^T \left[\mathbf{T}_{\mathrm{I}}^{\mathrm{C}}(\mathbf{r}_{\mathrm{GM}} + \mathbf{r}_{\mathrm{CG}})\times\right] \tag{22}$$

$$\frac{\partial u}{\partial \mathbf{r}_{\mathrm{CG}}} = \frac{\partial u}{\partial \mathbf{r}_{\mathrm{MC}}^{\mathrm{C}}} \frac{\partial \mathbf{r}_{\mathrm{MC}}^{\mathrm{C}}}{\partial \mathbf{r}_{\mathrm{CG}}} = -\mathbf{c}_1^T \mathbf{T}_{\mathrm{I}}^{\mathrm{C}} \tag{23}$$

$$\frac{\partial v}{\partial \mathbf{r}_{\mathrm{GM}}} = \frac{\partial v}{\partial \mathbf{r}_{\mathrm{MC}}^{\mathrm{C}}} \frac{\partial \mathbf{r}_{\mathrm{MC}}^{\mathrm{C}}}{\partial \mathbf{r}_{\mathrm{GM}}} = -\mathbf{c}_2^T \mathbf{T}_{\mathrm{I}}^{\mathrm{C}} \tag{24}$$

$$\frac{\partial v}{\partial \epsilon_{\mathrm{C}}} = \frac{\partial v}{\partial \mathbf{r}_{\mathrm{MC}}^{\mathrm{C}}} \frac{\partial \mathbf{r}_{\mathrm{MC}}^{\mathrm{C}}}{\partial \epsilon_{\mathrm{C}}} = \mathbf{c}_2^T \left[\mathbf{T}_{\mathrm{I}}^{\mathrm{C}}(\mathbf{r}_{\mathrm{GM}} + \mathbf{r}_{\mathrm{CG}})\times\right] \tag{25}$$

$$\frac{\partial v}{\partial \mathbf{r}_{\mathrm{CG}}} = \frac{\partial v}{\partial \mathbf{r}_{\mathrm{MC}}^{\mathrm{C}}} \frac{\partial \mathbf{r}_{\mathrm{MC}}^{\mathrm{C}}}{\partial \mathbf{r}_{\mathrm{CG}}} = -\mathbf{c}_2^T \mathbf{T}_{\mathrm{I}}^{\mathrm{C}} \tag{26}$$

where

$$\left[\mathbf{a}\times\right] = \begin{bmatrix} 0 & -a_3 & a_2 \\ a_3 & 0 & -a_1 \\ -a_2 & a_1 & 0 \end{bmatrix} \tag{27}$$

is the skew-symmetric matrix representation of the cross product for a vector $\mathbf{a}$.

The apparent diameter measurement is expressed as follows:

$$n_{\mathrm{d}} = \frac{2R_M f s}{\sqrt{r_{\mathrm{MC}}^2 - R_M^2}} \tag{28}$$

where n_{d} is the angular diameter of the Moon in pixels, R_M is the Moon radius, and r_{MC} is the distance between the Moon and camera. The variation of the angular diameter measurement is obtained as follows:

$$\delta n_{\mathrm{d}} = -\frac{r_{\mathrm{MC}} n_{\mathrm{d}}}{r_{\mathrm{MC}}^2 - R_M^2} \frac{(\mathbf{r}_{\mathrm{MC}}^{\mathrm{C}})^{\mathrm{T}}}{r_{\mathrm{MC}}} \delta \mathbf{r}_{\mathrm{MC}}^{\mathrm{C}} = \mathbf{d}^T \delta \mathbf{r}_{\mathrm{MC}}^{\mathrm{C}} \tag{29}$$

so that the partial for the apparent diameter measurement is described as:

$$\frac{\partial n_{\mathrm{d}}}{\partial \mathbf{r}_{\mathrm{GM}}} = \frac{\partial n_{\mathrm{d}}}{\partial \mathbf{r}_{\mathrm{MC}}^{\mathrm{C}}} \frac{\partial \mathbf{r}_{\mathrm{MC}}^{\mathrm{C}}}{\partial \mathbf{r}_{\mathrm{GM}}} = -\mathbf{d}^T \mathbf{T}_{\mathrm{I}}^{\mathrm{C}} \tag{30}$$

$$\frac{\partial n_{\mathrm{d}}}{\partial \epsilon_{\mathrm{C}}} = \frac{\partial n_{\mathrm{d}}}{\partial \mathbf{r}_{\mathrm{MC}}^{\mathrm{C}}} \frac{\partial \mathbf{r}_{\mathrm{MC}}^{\mathrm{C}}}{\partial \epsilon_{\mathrm{C}}} = \mathbf{d}^T \left[\mathbf{T}_{\mathrm{I}}^{\mathrm{C}}(\mathbf{r}_{\mathrm{GM}} + \mathbf{r}_{\mathrm{CG}})\times\right] \tag{31}$$

$$\frac{\partial n_{\mathrm{d}}}{\partial \mathbf{r}_{\mathrm{CG}}} = \frac{\partial n_{\mathrm{d}}}{\partial \mathbf{r}_{\mathrm{MC}}^{\mathrm{C}}} \frac{\partial \mathbf{r}_{\mathrm{MC}}^{\mathrm{C}}}{\partial \mathbf{r}_{\mathrm{CG}}} = -\mathbf{d}^T \mathbf{T}_{\mathrm{I}}^{\mathrm{C}} \tag{32}$$

The centroid and apparent diameter measurement noises are based on the one for Orion's Exploration Mission 1.[5] Measurement noise error models are expressed as follows:

$$\sigma_\alpha = \sqrt{(0.15\ \text{pix})^2 + \left(\frac{fs(2000\ \text{m})}{r_{\text{MC}}}\right)^2} \tag{33}$$

$$\sigma_\beta = \sqrt{(0.06\ \text{pix})^2 + \left(\frac{fs(2000\ \text{m})}{2r_{\text{MC}}}\right)^2} \tag{34}$$

$$\sigma_d = \sqrt{(0.12\ \text{pix})^2 + \left(\frac{fs(2000\ \text{m})}{r_{\text{MC}}}\right)^2} \tag{35}$$

where α and β indicate the parallel and perpendicular axes to the Moon-Sun direction, respectively, and σ_d is the resulting diameter error in pixels. The bias models are described as:

$$b_\alpha = (0.383\ \text{pix}) - \frac{1.058 \times 10^8\ \text{pix-m}}{r_{\text{MC}}} \tag{36}$$

$$b_\beta = 0\ \text{pix} \tag{37}$$

$$b_d = (-0.236\ \text{pix}) - \frac{5.986 \times 10^7\ \text{pix-m}}{r_{\text{MC}}} \tag{38}$$

The Orion camera model is used for this analysis which has a field of view of 20 × 16 degrees. Moreover, the camera misalignment and camera position biases are 45 arcsec and 0.3 m, 3σ, on each axis, respectively.

3.3 GPS Measurement Model

The Global Positioning System (GPS) is widely used to estimate states of a vehicle in low Earth orbit (LEO). However, the extension of GPS use into deep space has recently been studied, with for example, the Geostationary Operational Environmental Satellite R (GOES-R) and the Magnetospheric Multiscale Mission (MMS).[15–17] These two missions have shown that it is possible to receive a sidelobe or an edge of the main lobe of GPS signal that cross the Earth's limb. Moreover, simulations have shown that GPS use can be extended to lunar distances via a high-gain antenna. This study assumes use of a high-sensitivity GPS receiver, having a threshold of around 20 dB-Hz, and a high-gain antenna with a peak gain of 15 dB (corresponding to less than about 1 m in diameter).[9]

The pseudo-range measurement is modeled as follows:

$$\rho = \|\mathbf{r}_{\text{GE}} - \mathbf{r}_{\text{satE}}\| + \nu_\rho = \|\mathbf{r}_{\text{GM}} + \mathbf{r}_{\text{ME}} - \mathbf{r}_{\text{satE}}\| + \nu_\rho \tag{39}$$

where $\mathbf{r}_{\text{satE}}$ is the position vector of the observed satellite with respect to Earth in the inertial frame and v_ρ is the Gaussian measurement noise. Hence, the linear measurement model is obtained as

$$H(\bar{\mathbf{x}})\delta\mathbf{x} = \frac{(\bar{\mathbf{r}}_{\text{GM}} + \mathbf{r}_{\text{ME}} - \mathbf{r}_{\text{satE}})^{\text{T}}}{\|\bar{\mathbf{r}}_{\text{GM}} + \mathbf{r}_{\text{ME}} - \mathbf{r}_{\text{satE}}\|}\delta\mathbf{r}_{\text{GM}} \tag{40}$$

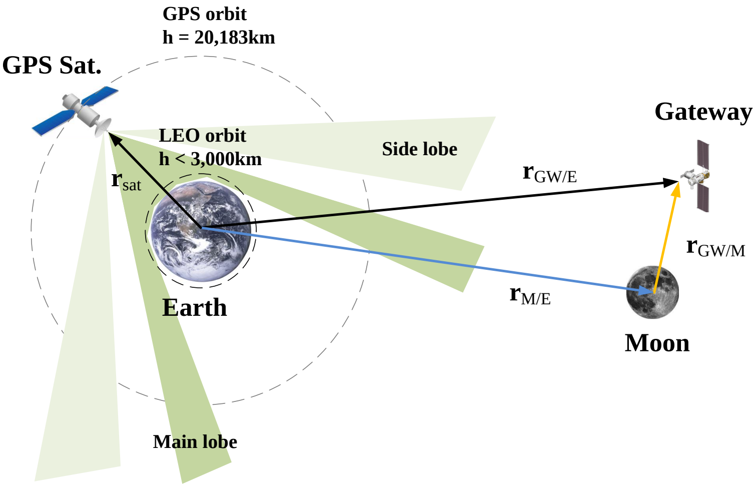

Fig. 4: Concept of GPS signal use at high altitude

The pseudo-range accuracy of the GPS measurement is 30 m, 3σ.[15] GPS satellite data is available using the SatNav ToolBox 2.0 for MATLAB. The ability to track sidelobes can contribute to the robustness and quality of the Gateway navigation. However, this paper only considers main lobe, which is designed to have a larger signal strength than the sidelobe signals. In addition, the sidelobe signals, which represent unwanted radiation in undesired directions, have not yet been fully characterized at high altitude. In other words, there are insufficient flight data to characterize the performance of sidelobe signals completely.[18] Since main lobe signal can extend to angles of up to 47°, the line of sight vector is limited less than 23.5° from the GPS satellite's antenna boresight.[17]

3.4 X-ray Measurement Model

Since X-ray pulsars are observed over the sky map and are of unique period and strength, X-ray pulsar navigation (XNav) has been proposed and used in a variety of studies.[19–21] XNav uses periodic X-ray pulsars emitted from a set of known pulsars in order to estimate the state of Gateway in deep space. Similar to DSN or GPS, X-ray sensors are used to compute the pulsar-based range measurements by comparing measured and predicted pulse time of arrival (TOA). However, XNav does not require assistance from any external navigation system.

The concept of XNav is shown in Figure 5 and is performed in an inertial system whose origin is the solar system barycenter (SSB). After receiving the X-ray pulse, the range measurement for Gateway to a reference point, $\mathbf{r}_G$,

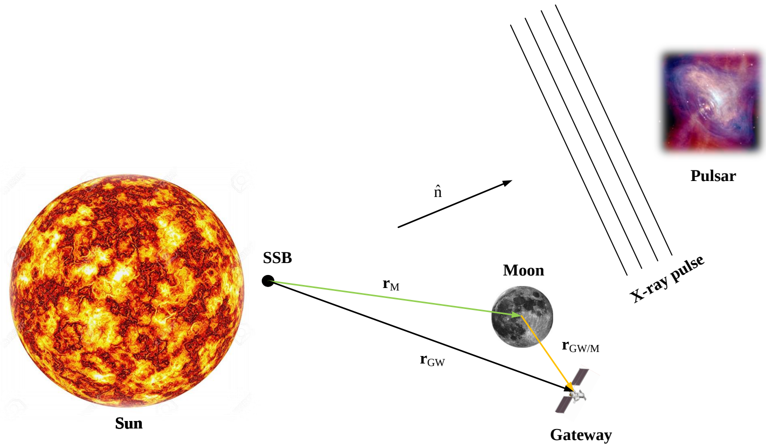

Fig. 5: Concept of X-ray pulsar navigation

is obtained by comparing the measured pulse TOA, t_{G}, at the vehicle to its predicted TOA, t_{SSB}, at the reference point.

$$t_{\mathrm{SSB}} = t_{\mathrm{G}} + \frac{\hat{\mathbf{n}}_i \cdot \mathbf{r}_{\mathrm{G}}}{c} + H.O.T. = t_{\mathrm{G}} + \frac{\hat{\mathbf{n}}_i}{c} \cdot (\mathbf{r}_M + \mathbf{r}_{\mathrm{GM}}) + H.O.T. \tag{41}$$

where $\hat{\mathbf{n}}_i$ is the unit vector to the selected i^{th} pulsar, c is the speed of light, and $\mathbf{r}_M$ is the position of the Moon with respect to the SSB. Since high order terms (H.O.T.) are several orders of magnitude smaller, only the first order terms are considered. If the position is defined as follows:

$$\mathbf{r}_{\mathrm{GM}} = \bar{\mathbf{r}}_{\mathrm{GM}} + \delta\mathbf{r}_{\mathrm{GM}} \tag{42}$$

then, Eq. (41) can be expressed in linear form with respect to $\delta\mathbf{r}_{\mathrm{GM}}$ as

$$c(t_{\mathrm{SSB}} - t_{\mathrm{G}}) - \hat{\mathbf{n}}_i\,(\mathbf{r}_M + \bar{\mathbf{r}}_{\mathrm{GM}}) = \hat{\mathbf{n}}_i \cdot \delta\mathbf{r}_{\mathrm{GM}} \tag{43}$$

Therefore, the linear measurement model of XNav can be constructed as

$$H(\bar{x})\delta\mathbf{x} = \hat{\mathbf{n}}_i \cdot \delta\mathbf{r}_{\mathrm{GM}} \tag{44}$$

The measurement noise is applied based on the accuracy from SEXTANT on-orbit results, which give a value of 10 km, 3σ.[21] The four best pulsars, based on dilution of precision (DOP), are selected as navigation pulsars, with those being: B0531+21, B0540-69, B1821-24, and B1937+21. The parameters of the pulsars are listed in Table 1.

Table 1: Characters of the candidate X-ray pulsars

Parameter	B0531+21	B0540-69	B1821-24	B1937+21
Galactic Latitude (°)	184.56	279.72	7.80	57.51
Galactic Longitude (°)	-5.78	-31.52	-5.58	-0.29
Right Ascension (°) (J2000)	83.63322	85.04667	276.13337	294.91067
Declination (°) (J2000)	22.01446	-69.33171	-24.86968	21.58309
Period (ms)	33.392	50.570	3.054	1.558

4 Simulation Results

LinCov analysis is conducted to evaluate the capability of onboard sensors for alleviating the load of DSN. LinCov analysis provides a means for predicting navigation performance using a single simulation, rather than a large number of Monte Carlo simulations, by directly propagating and updating the error covariance matrix P in Eq. (4).[11] The covariance propagation and update equations are expressed as follows:

$$P^{-}_{k|k-1} = F_{k-1} P^{+}_{k-1|k-1} F^{\mathrm{T}}_{k-1} + Q_{k-1} \tag{45}$$

$$P^{+}_{k|k} = P^{-}_{k|k-1} - K_k \left(H_k P^{-}_{k|k-1} H^{\mathrm{T}}_k + R_k \right) K^{\mathrm{T}}_k \tag{46}$$

where P^- and P^+ are the a priori and a posteriori covariance matrices, respectively. F and H are the Jacobian of the transition matrix and the measurement matrix evaluated at the nominal state, respectively. Q and R are the process and measurement noise covariance matrices, respectively. The Kalman gain, K, is calculated as

$$K_k = P^{-}_{k|k-1} H^{\mathrm{T}}_k \left(H_k P^{-}_{k|k-1} H^{\mathrm{T}}_k + R_k \right)^{-1} \tag{47}$$

The aforementioned four measurement types are utilized for this simulation and operational details for each measurement pass are as follows. In the absence of any onboard sensors, DSN measurements should be used at least 3 contacts per orbital period, lasting 6 hours each time, to meet the navigation performance requirements.[7] For this study, within an observation period, DSN range and range-rate measurements are available every 5 minutes and 1 minute, respectively. OpNav provides daily measurements every 30 seconds with a pass lasting 10 minutes. In addition, measurements are also taken right before the stationkeeping burns with a longer pass lasting 2 hours. The optical measurement time is scheduled to use the measurement only when a field of view is below 20 degrees. GPS measurements are assumed every 1 minute for the entire orbit. X-ray measurements are taken every 3 hours. The simulated results are shown for a duration of about five weeks.

Figure 6 shows the comparison of position and velocity navigation errors for each sensor for Gateway. The navigation errors peak at perilune when Gateway has the highest velocity. While it is crucial for requirements to be met around apolune, where correction maneuvers are performed, navigation requirements at perilune can be relaxed. For the OpNav and XNav cases, the position and velocity errors exceed the navigation requirement around perilune. In the GPS navigation case, the number of observable satellites vary from 0 to 3. Limited satellite observability is why the velocity error of Gateway with GPS navigation does not satisfy the requirement around perilune. On the other hand, DSN navigation satisfies the requirement over all times except for the first three days. The navigation error from propagation only, unaided by measurements, diverges (labeled as PureNav in the figure).

The navigation error of Gateway corresponding to combining DSN to any one of the other sensors is shown in Figure 7. When utilizing XNav or OpNav, the reliance on DSN can be reduced from six hours to five hours for each observation period in order to meet navigation error requirements. Moreover, the DSN measurement time can be reduced to four hours when using GPS in conjunction with DSN. Figure 8 shows the 3-σ values of Gateway navigation errors when using DSN in combination with two onboard sensors. The navigation performance of DSN with OpNav and XNav is almost the same as that of DSN with OpNav or with XNav, i.e. adding both provide only a marginal improvement. However, the reliance on DSN can be reduced by half, three hours, with GPS along with XNav and by two hours with GPS along with OpNav. The navigation performance of Gateway with all sensors is depicted in Figure 9. In that case, just a one hour pass is needed to meet the imposed navigation requirements rather than the six hours of DSN measurements alone. Results for reliance on DSN for each measurement pass for all onboard sensor configurations are summarized in Table 2 with the × symbol representing use of the associated sensor.

To analyze the contribution of different error groups to the total state estimation uncertainty at some point in time, an error budget is created for the last case where all sensors are used for the orbit determination.[22] Error groups are listed in Table 3. To establish the error budget, the same Kalman

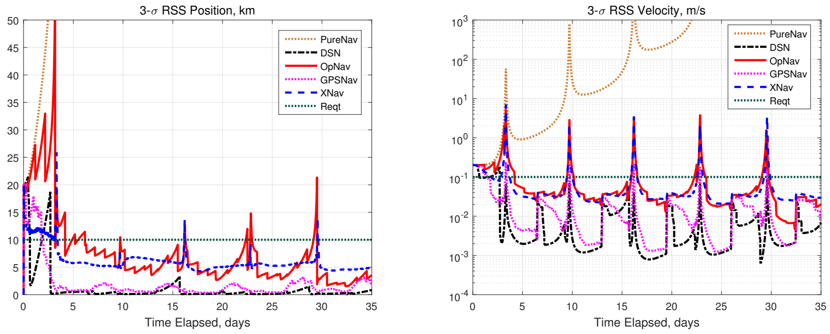

Position errors   Velocity errors

Fig. 6: Position and velocity error of Gateway with one sensor

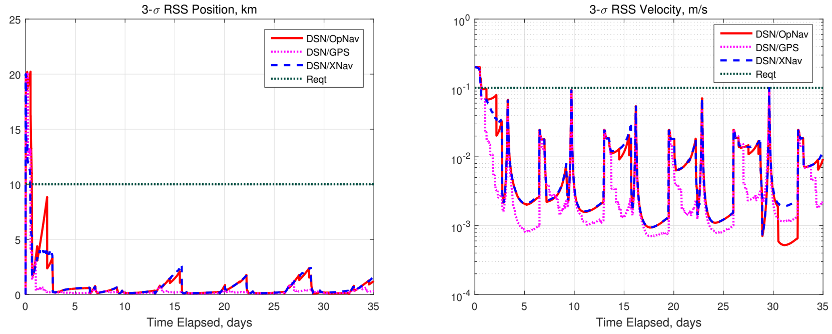

Position errors Velocity errors

Fig. 7: Position and velocity error of Gateway with two sensors

gain for the complete filter is used while only selected error groups are turned on in each simulation run. Table 4 shows the error budget when the navigation errors peak at the last perilune (at $t = 710$ hr). From the table, it can be seen that the GPS measurement noise affects the position and velocity errors the most for the peak at the last perilune.

The associate sensitivity analysis follows from the error budget analysis.[22] Error budget only shows the effects of using preassigned values of the error source statistics. In real life, however, the instrument performance (i.e. measurement noise) could be changed, thus affecting the navigation result. Therefore, the sensitivity of the measurement error groups to the overall state estimation uncertainty is computed by the sensitivity analysis. Each measurement error group is scaled along the desired test range from 0.1 to 10 for each simulation run. Then we replace the original contribution with the new one

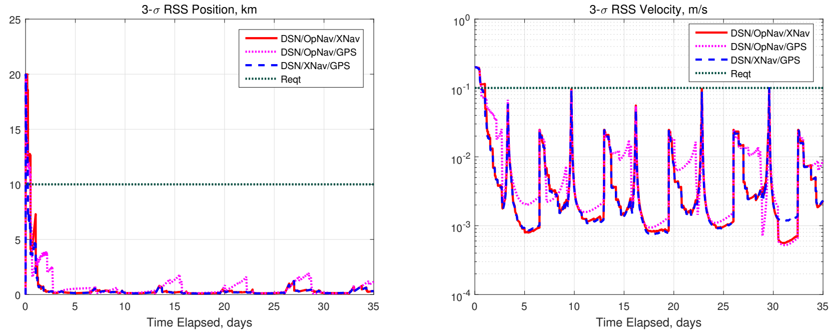

Position errors Velocity errors

Fig. 8: Position and velocity error of Gateway with three sensors

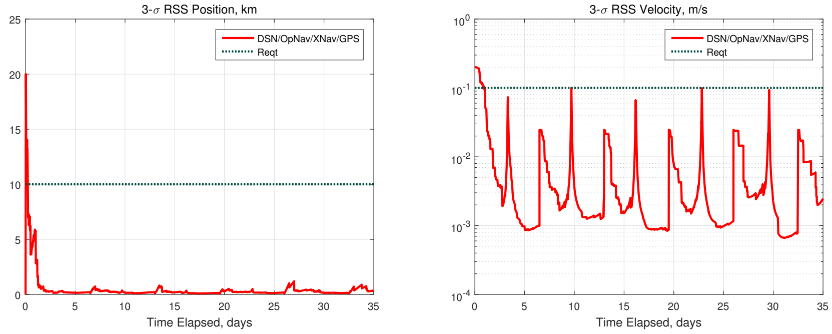

Position errors

Velocity errors

Fig. 9: Position and velocity error of Gateway with all sensors

and calculate the RSS values in the same way as the error budget analysis. The sensitivity curves are shown in Figure 10. It shows how each sensor group affects the state estimation uncertainty. The scaling of the GPS measurement noise causes the greatest increase in the overall estimation uncertainty, which means the estimate is most sensitive to the GPS measurement noise. On the other hand, the estimate is not sensitive to the X-ray measurement noise so that the X-ray measurement could be removed from the filter.

5 Conclusions

In this paper, three types of onboard sensors, a camera for Optical Navigation (OpNav) and antennas for GPS and X-ray pulsar Navigation (XNav), are analyzed to alleviate the reliance of Gateway on the Deep Space Network (DSN). Each measurement model for Gateway is described and linear covariance (LinCov) analysis is used to investigate more efficient ways to manage DSN resources. Numerical simulations are performed combining DSN measurements with all possible combinations of the other three sensors; showing the

DSN	OpNav	GPS	XNav	DSN measurement time (hrs)
×				6
×	×			5
×		×		4
×			×	5
×	×	×		2
×	×		×	5
×		×	×	3
×	×	×	×	1

Table 2: The capability of onboard sensors for alleviating the load of DSN

	Group #	Name
Initial Covariance	1	Position uncertainty
	2	Velocity uncertainty
	3	Camera misalignment uncertainty
	4	Camera position bias uncertainty
	5	GPS receiver clock bias uncertainty
Process Noise	6	Solar radiation pressure
	7	Station keeping burn imperfection
	8	Desaturation perturbation
Measurement Noise	9	DSN range measurement noise
	10	DSN range-rate measurement noise
	11	Camera measurement noise
	12	GPS measurement noise
	13	X-ray measurement noise

Table 3: Error group descriptions

Error group	Position (km)			Velocity (m/s)		
1	7.019e-07	6.112e-07	8.992e-07	2.317e-07	2.172e-07	2.497e-07
2	2.561e-07	3.767e-07	9.357e-07	2.220e-07	1.634e-07	6.294e-08
3	2.340e-05	8.033e-06	3.153e-05	6.609e-06	3.850e-06	7.330e-06
4	7.998e-05	2.978e-05	1.078e-05	9.348e-07	9.652e-06	2.081e-05
5	4.467e-10	7.020e-10	5.535e-10	3.881e-10	2.773e-10	3.944e-10
6	0.0033	0.0026	0.0031	9.589e-04	7.774e-04	8.277e-04
7	0.0043	0.0029	0.0029	9.212e-04	7.967e-04	0.0010
8	0.0018	6.296e-04	7.088e-04	1.473e-04	2.080e-04	4.749e-04
9	0.0085	0.0044	0.0030	0.0011	0.0015	0.0020
10	0.0087	0.0056	0.0053	0.0018	0.0015	0.0021
11	0.0454	0.0165	0.0076	0.0006	0.0053	0.0119
12	0.1001	0.0356	0.0202	0.0025	0.0116	0.0262
13	0.0048	0.0016	0.0013	0.0002	0.0005	0.0013
RSS	0.1108	0.0401	0.0229	0.0036	0.0130	0.0290

Table 4: Error budget

extent to which is possible to reduce the reliance on DSN. As data exchange and monitoring is done via DSN links, a system completely independent of ground communications is not desirable. It was found that the navigation performance of Gateway with combining DSN with either OpNav or XNav is similar as using DSN and the two sensors together, i.e. adding both only reduces the length of DSN passes by a fraction of one hour. Using GPS together with either OpNav or XNav alleviates the reliance on DSN in comparison with that of DSN with only GPS. Moreover, when all sensors are used for the orbit determination, dependency on DSN is limited to one hour per pass, a six-fold reduction from the nominal, DSN-only, approach. In addition, the error budget and sensitivity analysis indicates that the most significant error source for the orbit determination is the GPS measurement noise.

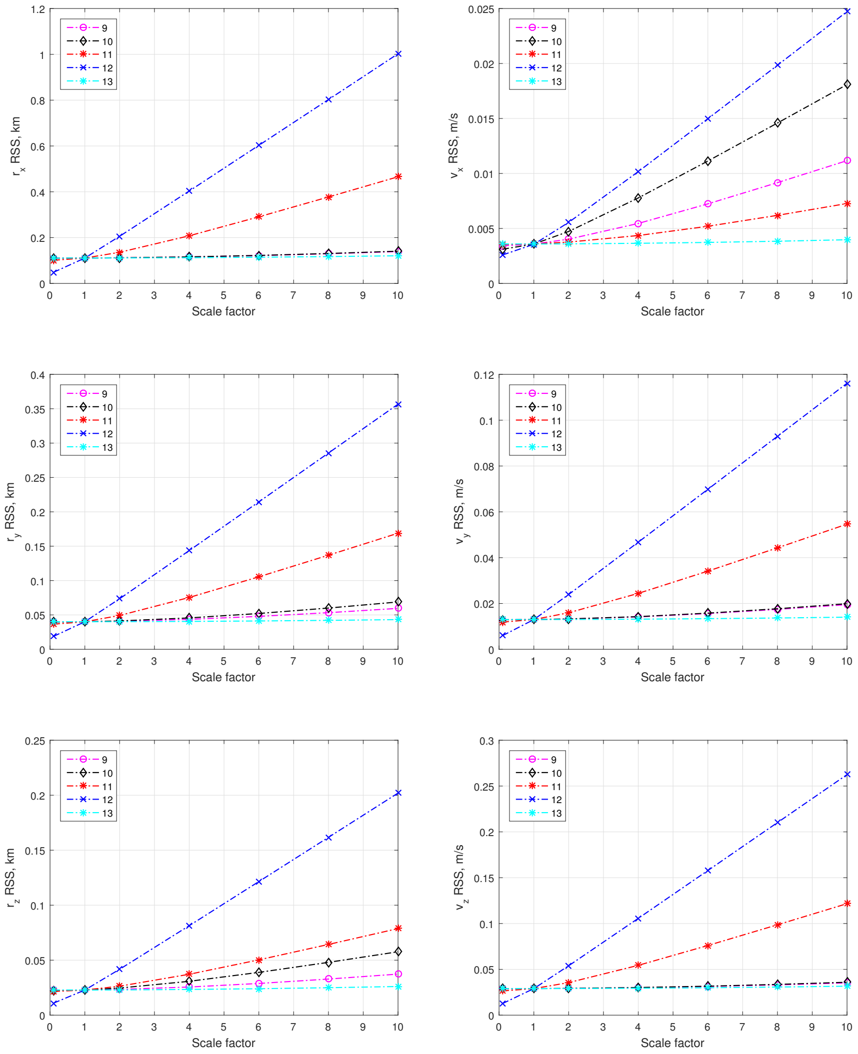

Position sensitivity analysis Velocity sensitivity analysis

Fig. 10: Sensitivity analysis

Aknowledgement

This work was sponsored in part by the NASA Johnson Space Center under contract number NNX17AI35A.

Conflict of Interest Statement

On behalf of all authors, the corresponding author states that there is no conflict of interest.

References

1. E. M. Zimovan, K. C. Howell, and D. C. Davis, "Near Rectilinear Halo Orbits and Their Application in Cis-Lunar Space," *3rd IAA Conference on Dynamics and Control of Space Systems, Moscow, Russia*, 2017.
2. S. E. Wolff, "Deep Space Network," 2003.
3. C. P. Newman, D. C. Davis, R. J. Whitley, J. R. Guinn, and M. S. Ryne, "Stationkeeping, Orbit Determination, and Attitude Control for Spacecraft in Near Rectilinear Halo Orbits," *AAS/AIAA Astrodynamics Specialist Conference, Snowbird, UT*, 2018. AAS 18-388.
4. S. I. Sheikh, D. J. Pines, P. S. Ray, K. S. Wood, M. N. Lovellette, and M. T. Wolff, "Spacecraft navigation using X-ray pulsars," *Journal of Guidance, Control, and Dynamics*, Vol. 29, No. 1, 2006, pp. 49–63.
5. G. N. Holt, C. N. D'Souza, and D. W. Saley, "Orion Optical Navigation Progress Toward Exploration Mission 1," *28th 2018 Space Flight Mechanics Meeting, Kissimmee, FL*, 2018. doi: 10.2514/6.2018-1978.
6. C. P. Newman, R. Sieling, D. C. Davis, and R. J. Whitley, "Attitude Control and Orbit Determination of a Crewed Spacecraft With a Lander in Near Rectilinear Halo Orbit," *29th AAS/AIAA Space Flight Mechanics Meeting, Ka'anapali, Maui, HI*, 2019. AAS 19-545.
7. J. R. Guinn, S. Bhaskaran, T. A. Ely, B. M. Kennedy, T. J. Martin-Mur, R. S. Park, J. E. Riedel, D. C. Roth, and A. T. Vaughan, "The Deep Space Positioning System (DPS) Navigator Concept for the Lunar Gateway," *42nd Annual AAS Guidance and Control Conference, Breckenridge, CO*, 2019. AAS 19-093.
8. J. S. Parker, J. Smith, A. Forsman, C. Rabotin, C. Cain, and B. Cheetham, "The Cislunar Autonomous Positioning System (CAPS)," *42nd Annual AAS Guidance and Control Conference, Breckenridge, CO*, 2019. AAS 19-094.
9. Y. Nakajima, T. Yamamoto, and H. Ikeda, "Using GNSS Receiver at Near Rectlinear Halo Orbit," *29th AAS/AIAA Space Flight Mechanics Meeting, Ka'anapali, Maui, HI*, 2019. AAS 19-276.
10. S. Bhatt, S. Steffes, and G. Barton, "A Deep Space Autonomous Navigation System for the Lunar Orbital Platform-Gateway," *42nd Annual AAS Guidance and Control Conference, Breckenridge, CO*, 2019. AAS 19-092.
11. P. S. Maybeck, *Stochastic Models, Estimation, and Control.* New York, NY: Academic Press, 1979. ISBN: 978-0-12-411042-7.
12. D. K. Geller, "Linear Covariance Techniques for Orbital Rendezvous Analysis and Autonomous Onboard Mission Planning," *Journal of Guidance Control and Dynamics*, Vol. 29, November-December 2006, pp. 1404–1414.
13. C. H. Acton Jr, "Ancillary data services of NASA's navigation and ancillary information facility," *Planetary and Space Science*, Vol. 44, No. 1, 1996, pp. 65–70.
14. C. D?Souza and G. Barton, "Process Noise Assumptions for Orion Cislunar Missions," *NASA MPCV Technical Brief*, 2016.
15. L. B. Winternitz, W. A. Bamford, S. R. Price, J. R. Carpenter, A. C. Long, and M. Farahmand, "Global Positioning System Navigation Above 76,000 KM for NASA'S Magnetospheric Multiscale Mission," *NAVIGATION: Journal of The Institute of Navigation*, Vol. 64, No. 2, 2017, pp. 289–300.
16. B. W. Ashman, F. H. Bauer, J. J. K. Parker, and J. E. Donaldson, "GPS Operations in High Earth Orbit: Recent Experiences and Future Opportunities," *2018 SpaceOps Conference, Marseille, France*, 2018. AIAA 2018-2568, doi: 10.2514/6.2018-2568.

17. B. W. Ashman, J. J. K. Parker, F. H. Bauer, and M. Esswein, “Exploring the Limits of High-Altitude GPS for Future Lunar Missions,” *41st Annual AAS Guidance and Control Conference, Breckenridge, CO*, 2018. AAS 18-082.
18. J. J. K. Parker, J. E. Valdez, F. H. Bauer, and M. C. Moreau, “Use and Protection of GPS Sidelobe Signals for Enhanced Navigation Performance in High Earth Orbit,” *39th Annual AAS Guidance and Control Conference, Breckenridge, CO*, 2016. AAS 16-72.
19. S. I. Sheikh, D. J. Pines, P. S. Ray, K. S. Wood, M. N. Lovellette, and M. T. Wolff, “Spacecraft Navigation Using X-Ray Pulsars,” *Journal of Guidance, Control, and Dynamics*, Vol. 29, No. 1, 2006, pp. 49–63. doi: 10.2514/1.13331.
20. A. A. Emadzadeh and J. L. Speyer, *Navigation in Space by X-ray Pulsars*. New York, NY: Springer-Verlag New York, 2011. doi: 10.1007/978-1-4419-8017-5.
21. L. B. Winternitz, M. A. Hassouneh, J. W. Mitchell, S. R. Price, W. H. Yu, S. R. Semper, P. S. Ray, K. S. Wood, Z. Arzoumanian, and K. C. Gendreau, “SEXTANT X-ray Pulsar Navigation Demonstration: Additional On-Orbit Results,” *2018 SpaceOps Conference, Marseille, France*, 2018. AIAA 2018-2538, doi: 10.2514/6.2018-2538.
22. O. Awad and R. H. Bishop, “A Multiplicative Extended Kalman Filter for Low Earth Orbit Attitude Estimation Aboard a 0.5U SmallSat,” *43th Annual AAS Guidance and Control Conference, Breckenridge, CO*, 2020. AAS 20-027.